Lee *Earth, Planets and Space* [redacted]
DOI 10.1186/s40623-015-0337-5

Earth, Planets and Space
a SpringerOpen Journal

FULL PAPER Open Access

Numerical earthquake model of the 20 April 2015 southern Ryukyu subduction zone M6.4 event and its impact on seismic hazard assessment

Shiann-Jong Lee

Abstract

The M6.4 earthquake that took place on the 20 April 2015 off the shore of eastern Taiwan was the largest event in the vicinity of Taiwan during 2015. The mainshock was located in the southern Ryukyu subduction zone, which is the interface between the Philippine Sea Plate and the Eurasian Plate. People in Taipei experienced strong ground shaking for more than 40 s, even though the epicenter was located more than 150 km away. In order to understand the origin of ground motions from this earthquake and how it caused such strong shaking in Taipei, a numerical earthquake model is analyzed, including models of source rupture and wave propagation. First, a joint source inversion was performed using teleseismic body wave and local ground motion data. Source inversion results show that a large slip occurred near the hypocenter, which rapidly released seismic energy in the first 2 s. Then, the rupture propagated toward the shallow fault plane. A large amount of seismic energy was released during this rupture stage that slipped for more than 8 s before the end of the rupture. The estimated stress drop is 2.48 MPa, which is consistent with values for subduction zone earthquakes. Forward simulation using this inverted source rupture model and a 3D seismic velocity model based on the spectral-element method was then performed. Results indicate that the strong ground motion in Taipei resulted from two factors: (1) the Taipei basin amplification effect and (2) the specific source radiation pattern. The results of this numerical earthquake model imply that future subduction zone events that occur in offshore eastern Taiwan are likely to cause relatively strong ground shaking in northern Taiwan, especially in the Taipei metropolitan area.

Keywords: Ryukyu subduction zone; Source rupture process; Source radiation; Ground motion simulation; Basin effect

Background

On the 20 April 2015, a moderately large earthquake with a magnitude of M_L 6.38 (M_w 6.4) struck offshore eastern Taiwan (hereafter referred to as the 0420 earthquake). The earthquake report of the Central Weather Bureau (CWB) showed an epicenter located at 122.441° E/24.022° N with a hypocentral depth of 30.57 km. The mainshock was close to Yilan county (about 80 km from the epicenter), where a CWB intensity scale of 4 (25–80 gal) was experienced. A CWB intensity of 4 was also recorded in Taipei City, even though it is located over 150 km from the epicenter. People in Taipei experienced strong long-period ground shaking for more than 40 s. After the earthquake, the Japan Meteorological Agency immediately issued an alert for the southern Okinawa island chain regarding a possible 1-m tsunami, but the alert was lifted after an hour, with no sign of high waves or damage. Unfortunately, the strong ground shaking of this event caused the indirect death of one person and injuries to several others in Taiwan.

The 0420 earthquake occurred in a seismically active area, where several moderate-to-large earthquakes have been recorded in the past 10 years (see Fig. 1 and Table 1). On 31 March 2002, an M_w 7.1 (M_L 6.8) earthquake, called the 331 Hualien offshore earthquake, occurred in this area. This was the largest event in Taiwan since the 1999 Chi-Chi earthquake (M_w 7.6). Again,

Correspondence: sjlee@earth.sinica.edu.tw
Institute of Earth Sciences, Academia Sinica, Taipei, Taiwan

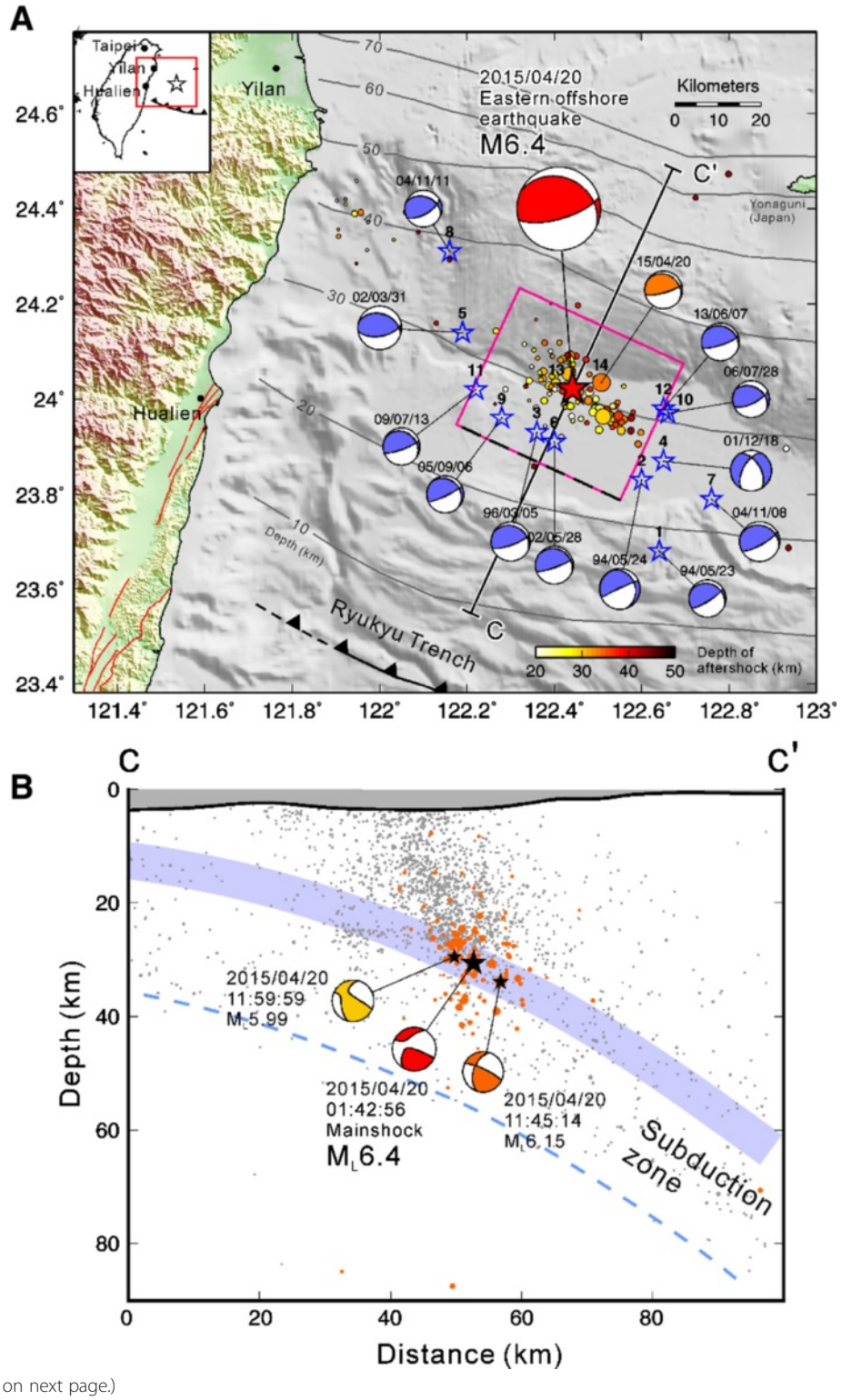

Fig. 1 (See legend on next page.)

(See figure on previous page.)
Fig. 1 The 20 April 2015 eastern offshore earthquake. **a** The location of the 20 April 2015 Ryukyu subduction zone earthquake. The *red star* indicates the epicenter of the 0420 event. The aftershocks of the 0420 events are shown by the *warm colored circles*. The epicenters of the 1994 to 2013 $M_L > 6$ events are shown by the *blue open stars* (see also Table 1). The *open pink rectangle* indicates the surface projection of the fault model, with its shallowest portion indicated with a *black dashed line*. The *gray lines* display the depths of the subducting plate in this area (Wu et al., 2009). Detailed source parameters of major earthquakes occurring in offshore eastern Taiwan recorded in the last 10 years are provided in Table 1. **b** Cross section along the C–C' profile. *Blue thick line* and *dotted line* indicate the plate interface and the bottom of Benioff zone, respectively. The *beach balls* show the focal mechanisms of the 0420 mainshock and two largest aftershocks. The aftershocks of the 0420 events are shown by the *orange circles*. The *gray dots* denote background seismicity ($M > 3$) recorded from 1990 to 2013, as reported by the CWB

although the hypocentral distance to Taipei was more than 100 km, people in the city felt very strong ground shaking with a long duration (Chen et al., 2003; Huang et al., 2010). This event caused two cranes to collapse from the Taipei 101 construction site, resulting in the deaths of two people as well as several injuries.

The centroid moment tensors (CMT) of the 0420 earthquake provided by the Real-time Moment Tensor (RMT) Monitoring System (Lee et al., 2013) showed thrust faulting mechanisms with two west–east striking nodal planes, one dipping toward the north with a shallower dipping angle, and the other dipping toward the south with a steeper fault plane (Fig. 1). Several noticeable aftershocks were recorded after the mainshock. The largest aftershock (M_L 6.15) occurred around 10 h after the mainshock. The epicenters of this earthquake sequence follow a northwest-to-southeast alignment (Fig. 1). On the vertical profile (C–C' in Fig. 1), the patterns of aftershock distributions appear to be consistent with the background seismicity, which presents a clear northward-dipping subduction Benioff zone. In addition, the depth of the 0420 event (30.57 km) also fits well with the fault geometry of the subducting plate in this area (Wu et al., 2009). From this information, the 0420 event is likely to be an inter-plate earthquake of the Ryukyu subduction zone, which lies at the boundary between the Philippine Sea Plate and the Eurasian Plate.

Hsu et al. (2012) proposed that the southernmost Ryukyu subduction zone needs to consider the potential M_w 7.5–8.7 tsunami earthquakes generated by shallow ruptures. Nakamura (2014) used seismic tomography and receiver function analysis to investigate the relation between the slab structure in the southern Ryukyu arc region and the occurrence of slow-slip events that repeat biannually. Result suggests that the thermal condition of the southern Ryukyu arc is similar to the case of a hot-slab area where slow-slip events occur. The repeated occurrence of slow-slip event results in stress accumulation in the up-dip part of the fault, which could potentially induce megathrust earthquakes. Lin et al. (2014) indicated that the occurrence of a potential Sumatra-like earthquake in the south Ryukyu arc is highly likely and

Table 1 List of $M_L > 6$ earthquake events in offshore eastern Taiwan, recorded between 1994 and 2015

No.	Date (yyyy/mm/dd)	Time (hh:mi:ss)	Long. (°E)	Lat. (°N)	Depth (km)	Strike (°)	Dip (°)	Rake (°)	M_L
1	1994/05/23	15:16:58	122.64	23.68	5.54	292	21	142	6.00
2	1994/05/24	04:00:40	122.60	23.83	4.45	245	87	−66	6.60
3	1996/03/05	14:52:27	122.36	23.93	6.00	296	21	134	6.40
4	2001/12/18	04:03:00	122.65	23.87	12.00	209	58	−46	6.70
5	2002/03/31	06:52:49	122.19	24.14	13.81	287	35	112	6.80
6	2002/05/28	16:45:14	122.40	23.91	15.23	300	15	139	6.20
7	2004/11/08	15:54:55	122.76	23.79	10.00	290	21	137	6.58
8	2004/11/11	02:16:44	122.16	24.31	27.26	289[a]	36[a]	133[a]	6.09
9	2005/09/06	01:16:00	122.28	23.96	16.76	313	20	157	6.00
10	2006/07/28	07:40:10	122.66	23.97	27.97	299	33	139	6.02
11	2009/07/13	18:05:02	122.22	24.02	18.08	305	21	143	6.00
12	2013/06/07	16:38:02	122.65	23.98	35.32	296	18	133	6.21
13	2015/04/20	01:42:56	122.44	24.02	30.57	295[b]	26[b]	128[b]	6.38
14	2015/04/20	11:45:13	122.51	24.04	33.87	305[b]	20[b]	139[b]	6.15

Event times, locations, and magnitudes are taken from the CWB earthquake catalogue. The focal mechanisms are derived from the US Geological Survey CMT solution

[a]The focal mechanism is derived from the Broadband Array in Taiwan for Seismology CMT solution

[b]The focal mechanism is derived from the Real-time Moment Tensor Monitoring System

the rupture will mainly propagate continentward to fulfill the region of low seismicity. Thus, investigating the origin of the 0420 event and how it caused strong ground shaking in the Taipei metropolitan area is an important topic for scientific research, since it could be an indication of future hazardous large subduction zone events.

This study analyzes a numerical earthquake model of the 0420 event. The numerical earthquake model includes models of source rupture and 3D wave propagation. The entire time history of earthquake is going to be rebuilt through fully 3D simulations based on advanced numerical methods in computational seismology. Both the inverse (source inversion) and forward (ground motion simulation) studies are performed with parallel computing techniques to improve computing performance and enhance the resolution of model in both time and space. First, source rupture process analysis is carried out using joint source inversion. Then, the inversion result is considered as the input source model for a forward ground motion simulation. Since the same regional 3D Green's function is employed in the source inversion and ground motion simulation, the 3D path effects are identical and well included in both the inverse and forward processes. Finally, the origin of the prolonged strong ground shaking in Taipei during this event and its impact on seismic hazard assessment are discussed.

Source rupture model

Data

To understand the mechanisms of the 0420 earthquake, the rupture processes were investigated using joint source inversion. Two data sets were used in the inversion: teleseismic body wave (P wave) and regional strong ground motion data (P, S, and surface waves). The teleseismic data have good data quality and azimuthal coverage of the earthquake, which provides a first-order determination of fault rupture behavior. A total of 42 teleseismic stations were used for the 0420 event (Fig. 2). The stations provided good azimuthal coverage and were located between 30° and 90° to avoid the complex earth structure. These data comprised digital recordings obtained from the Incorporated Research Institutions for Seismology (IRIS). Signals were deconvolved from the instrument response and re-sampled to 10 points per second, and a band-pass filter (0.01 to 0.5 Hz) was applied. A time window of 40 s after the P arrival time was used, with an additional 10 s before the P arrival. The event was also well recorded by dense regional seismic networks (the CWB 24-bit Real-time Seismic Monitoring Network). Unfortunately, this data set cannot provide good azimuthal coverage around the source area, since all the stations are located on land (Fig. 2). However, additional source rupture process information can still be retrieved from the regional full-waveform seismic data. The vertical component of velocity waveform records were considered in the inversion. All strong motion data were integrated from acceleration to velocity, and then a band-pass filter was applied between 0.02 and 0.1 Hz. In total, 27 records were selected for the 0420 event. A waveform time window of 100 s was used, starting from the origin time of the event with a sampling rate of 0.1 s. All the P, S (SV), and surface waves are contained in this time window, and their influence on the inversion result is naturally included. As the epicenter was located far away from the island, GPS coseismic deformation data did not have sufficient signal-to-noise ratio to be included in the joint inversion.

Method

The finite fault source inversion problem is typically formulated in a linear form, $Ax = b$, where A is the matrix of Green's functions, b is the observed data vector, and x is the solution vector of slip characteristics on each subfault, including amplitude and direction (Hartzell and Heaton, 1983). The multiple-time windows technique was applied in the inversion procedure to provide a more detailed spatial and temporal resolution of the slip. The performance of the program was improved by using a parallel non-negative least-squares inversion technique (Lee et al., 2006). A misfit function used to evaluate the quality of a solution was defined as:

$$(Ax-b)^2/b^2 \quad (1)$$

In matrix A, the teleseismic P wave Green's functions were calculated using the approach developed by Kikuchi and Kanamori (1982), where the near source structure was given by a 1D average crust model of Taiwan (Chen and Shin, 1998) while the receiver side structure used a global 1D IASPEI91 model (Kennett and Engdahl, 1991). The teleseismic synthetic waveforms were filtered between 0.01 and 0.5 Hz. The 3D synthetic Green's functions for near-field ground motion stations were generated using the spectral-element method (SEM) (Komatitsch and Tromp 1999; Komatitsch et al. 2004), with a tomography velocity model taken from Huang et al. (2014). A complete description of the SEM mesh model is provided in the next section. Due to the lack of detailed 3D velocity structure in offshore eastern Taiwan, a lower frequency band was considered. The seismic synthetic waveforms were filtered between 0.02 and 0.1 Hz in the same frequency range as for the observed data. Lee et al. (2014) proposed that even in a lower frequency band, the full-waveform regional seismic data can still provide constraints for the source rupture process in both the spatial and temporal distributions of the slip.

In the inversion, 16 time windows of 0.8 s in length are used, each window overlapping by 0.4 s, leading to

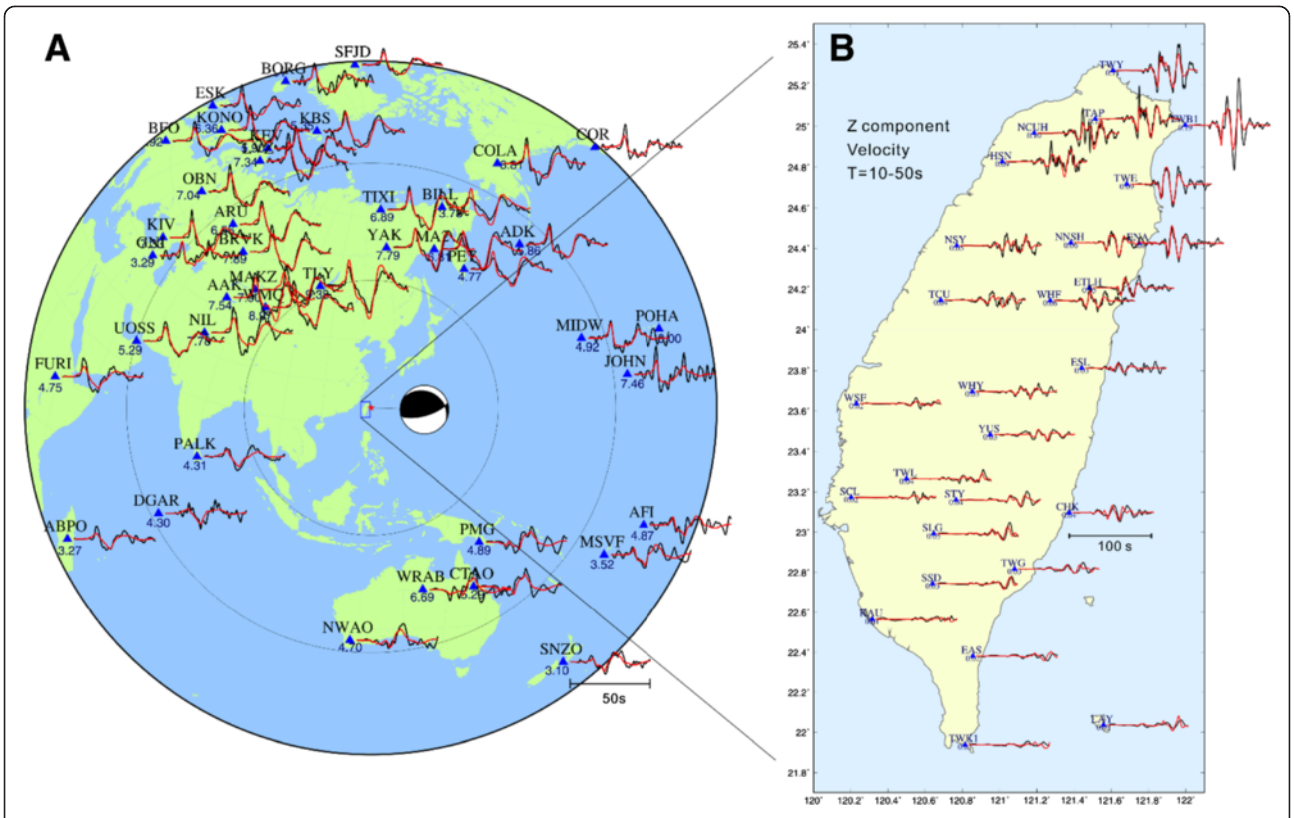

Fig. 2 The stations used in the source inversion and waveform comparisons between synthetics and observations. **a** Teleseismic body waves (P wave), and **b** local strong motion waveforms. *Black lines* are observations, and *red lines* are synthetics. The number beneath the station (*blue triangle*) indicates the peak value of observation. For the teleseismic waveform, both the synthetics and observations were employed a band-pass filter between 0.01 and 0.5 Hz. For the local strong motion data, the vertical component waveforms were integrated from acceleration to velocity and then a band-pass filter was applied between 0.02 and 0.1 Hz. The waveform misfits of the teleseismic and local strong motion data are 0.20 and 0.38, respectively

each subfault having a possibility to slip within 6.8 s after the rupture begins. A maximum rupture velocity, $V_r = 3.0$ km/s, was assumed; thus, the inverted rupture velocity will be between 0 and 3 km/s. A northwest–southeast strike and northern dipping fault plane characterized by thrust movement (strike 295°, dip 26°, and rake 128°) taken from the RMT (Lee et al., 2013) were considered. The fault planes were divided into 156 subfaults, each with a size of 3×3 km^2. The slip on each subfault was divided into rake ± 45° in the inversion. By doing so, the variation of rake angle in each subfault can be determined by the combination of these two slip components. To determine the slip amplitude from the inverted seismic moment, the empirical relationships between μ, V_p, V_s, and density (Brocher, 2005) were used to generate shear modulus on each subfault.

Results

The inversion results of the data fitting for the 0420 event are shown in Fig. 2. The inverted teleseismic synthetic waveform compared with observed data showed that the peak amplitudes and later phases fit sufficiently well (Fig. 2a). The teleseismic waveform misfit determined from Eq. (1) is 0.20. The regional synthetic waveforms versus observed velocity waveforms are shown in Fig. 2b. Most of major phases can be explained not only for stations near the source area but also for the stations far from it. However, some shifts in time can be found, especially for the stations located in southern Taiwan. The regional ground motion waveform misfit is 0.38.

Slip distribution determined from the joint source inversion for the 0420 events is shown in Fig. 3. The rupture of the 0420 event mainly occurred in a 15×15 km^2 area that had an irregular shape in which at least two asperities were identified. The initial rupture developed in a deeper part at a depth of around 30 km in the hypocenter. This area had the largest slip on the fault, with a maximum slip of 82.3 cm, and it was also identified as the first asperity. Slips in this rupture area were predominately right-lateral thrust movements. At the upper-left of the hypocenter, another large slip area that had more thrust movement compared to the hypocentral area can be observed. This is the second asperity, with a slip of around 50 cm. Some slip patches can be found around these two asperities, but their slips were relatively small.

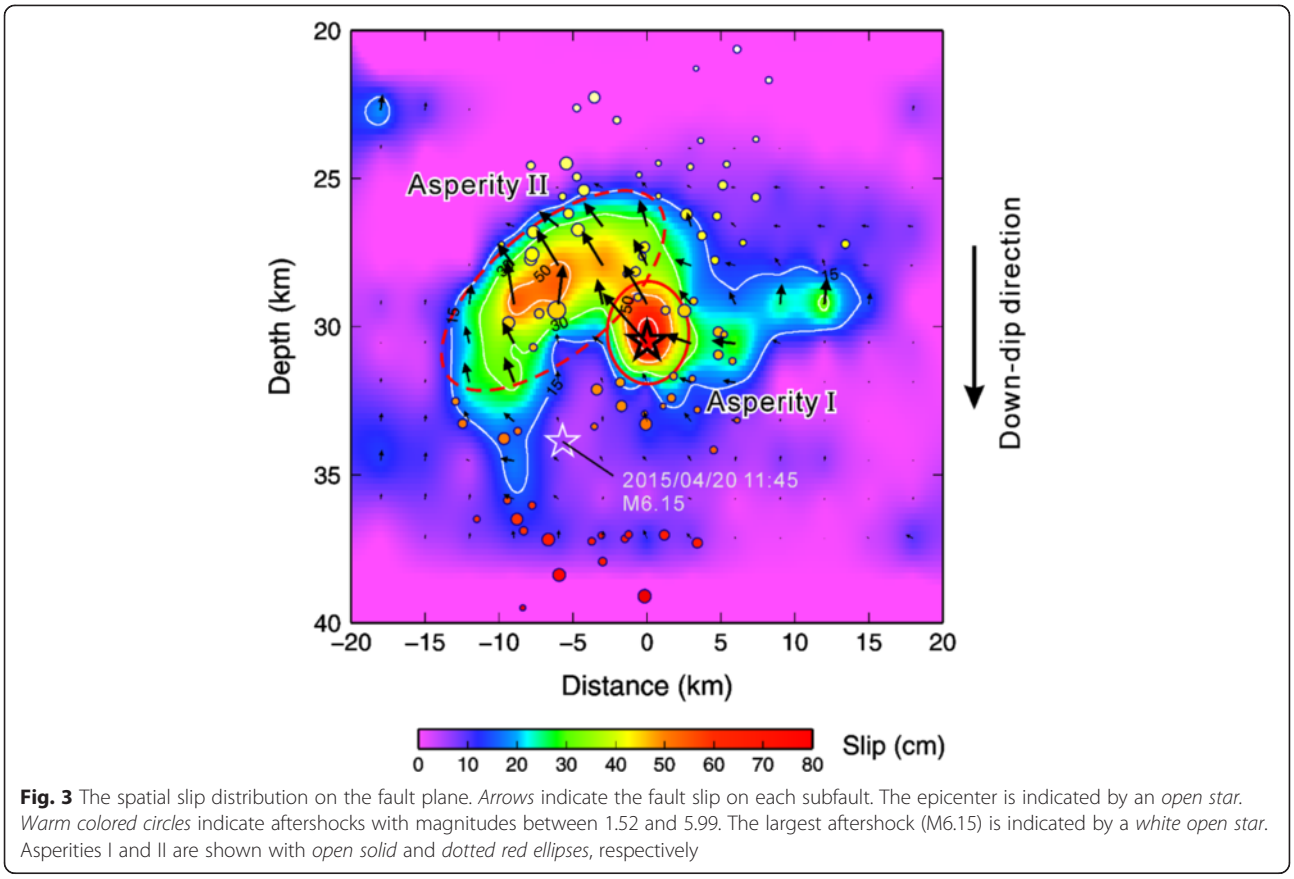

Fig. 3 The spatial slip distribution on the fault plane. *Arrows* indicate the fault slip on each subfault. The epicenter is indicated by an *open star*. *Warm colored circles* indicate aftershocks with magnitudes between 1.52 and 5.99. The largest aftershock (M6.15) is indicated by a *white open star*. Asperities I and II are shown with *open solid* and *dotted red ellipses*, respectively

The average slip on the fault plane determined from the joint inversion was approximately 24.6 cm. Most of the aftershocks occurred around this irregular slip area, and there were almost no aftershocks located inside the large slip area of the two asperities. From the map of the fault projected onto the seabed, both slip and aftershock distributions show a northwest–southeast trend (Fig. 4). The large slip area originated from the mainshock epicenter (Asperity I) and extended to the southeastern part (Asperity II) that moved toward the southeast predominantly by right-lateral thrust slip. The largest aftershock (M_L 6.15) was located in the deeper part of the fault plane, where the slip was relatively small during the mainshock.

The rupture snapshot shows that the rupture initiated from the hypocenter at a depth of around 30 km (Fig. 5). Within the first 2 s, a large amount of slip rapidly occurred in and around the hypocenter, which resulted in the first asperity on the fault plane. Then the rupture propagated to the shallower part (~25 km) in a southeastern direction. The slip accumulated slowly so that it ruptured for a long time, from 2 to 9 s, and became the second asperity. Figure 6 depicts the moment rate function, which shows there were rapid seismic energy releases in the first 2 s as a result of the first asperity. Then a large amount of seismic energy is released during the period from 2 to 9 s, which corresponds to the development of the second asperity. The source time function of the entire rupture was approximately triangular in shape with duration of around 10 s. The total seismic moment was 0.474×10^{19} Nm, which is equivalent to an earthquake of M_w 6.38. Assuming a circular fault model, the estimated stress drop $\Delta\sigma$ of the 0420 event was 2.48 MPa, which is consistent with the values for subduction zone earthquakes (Kanamori and Anderson, 1975; Allmann and Shearer, 2009).

Wave propagation model

Method

The source model derived from joint inversion was adopted to perform a forward 3D ground motion simulation based on the SEM. In the past studies, source inversion and forward wave propagation are typically carried out individually and use different velocity structure models (Sørensen et al., 2007; Bjerrum et al., 2010; Maeda et al., 2013). In this study, to ensure path effects are identical in the inversion and forward processes, the same SEM mesh and velocity model are used in both inverse and forward ground motion simulations.

The SEM mesh model employed is shown in Fig. 7. The size of the region is 466.01 × 548.39 km horizontally

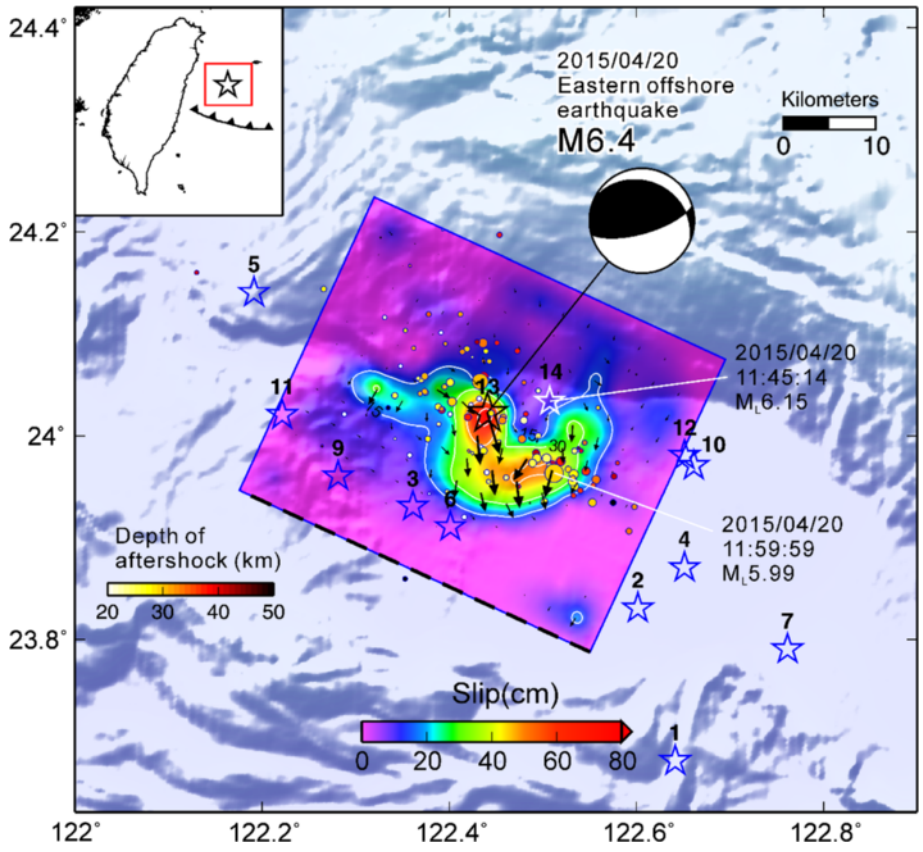

Fig. 4 Map of the slip distribution projected onto the seabed surface. The epicenter is indicated by a *black open star* and the largest aftershock is marked by a *white open star*. *Black arrows* indicate the fault slip on each subfault. *Warm colored circles* indicate aftershocks with magnitudes between 1.52 and 5.99. *Blue open stars* are the epicenters of the 1994 to 2013 $M_L > 6$ events listed in Table 1. The *beach balls* show the focal mechanisms determined by the RMT

and +3.93 to −180.00 km vertically. This model covers most of the land and offshore areas of Taiwan, which is capable of handling large earthquakes from offshore regions like 0420 event. Most of the currently available relevant seismological and geological information have incorporated in the model, including surface topography, shallow sedimentary (V_s 30; Kuo et al., 2012), and large-scale 3D wave-speed heterogeneity information. The surface topography based on 40-m digital elevation model data is implemented at the top of the SEM mesh model (Lee et al., 2009). The 3D regional tomographic model was derived by Huang et al. (2014) which is based on a joint inversion scheme, integrating the data of P and S wave travel times, S–P times, and the borehole logging data (V_s 30 for near-surface correction) into one system. The Taipei basin geometry was not incorporated in the mesh since it is too shallow (<1 km). The total number of elements and Gauss-Lobatto-Legendre (GLL) points are 753408 and 51090336, respectively. The distances between GLL points in the horizontal direction at the surface is approximately 303.4 m. Considering the resolutions of the numerical mesh and the velocity models used, the simulation is capable of representing a 3D wavefield and synthetic waveforms that are accurate to 0.625 Hz. It requires 288 CPU cores and takes about 8 h to complete a 140 s ground motion simulation. The simulations were carried out on Green cluster in the Institute of Earth Sciences, Academia Sinica. Although the maximum frequency of the local waveforms used in the source inversion is 0.1 Hz, it is still possible to have higher frequency information that results from the teleseismic data (0.01 to 0.5 Hz) and path effects involved in forward simulations, such as high-frequency scattering due to surface topography.

Results

Snapshots of the simulation for the three components of the velocity wavefield are shown in Fig. 8. An additional movie file shows this in more detail (see Additional file 1). Within the first 15 s, a large number of seismic waves were excited from the source area as a result of the development of the rupture on the fault plane. During this time period, ground motion on the seabed was dominated by source effects. At about 25 s, the P wave front

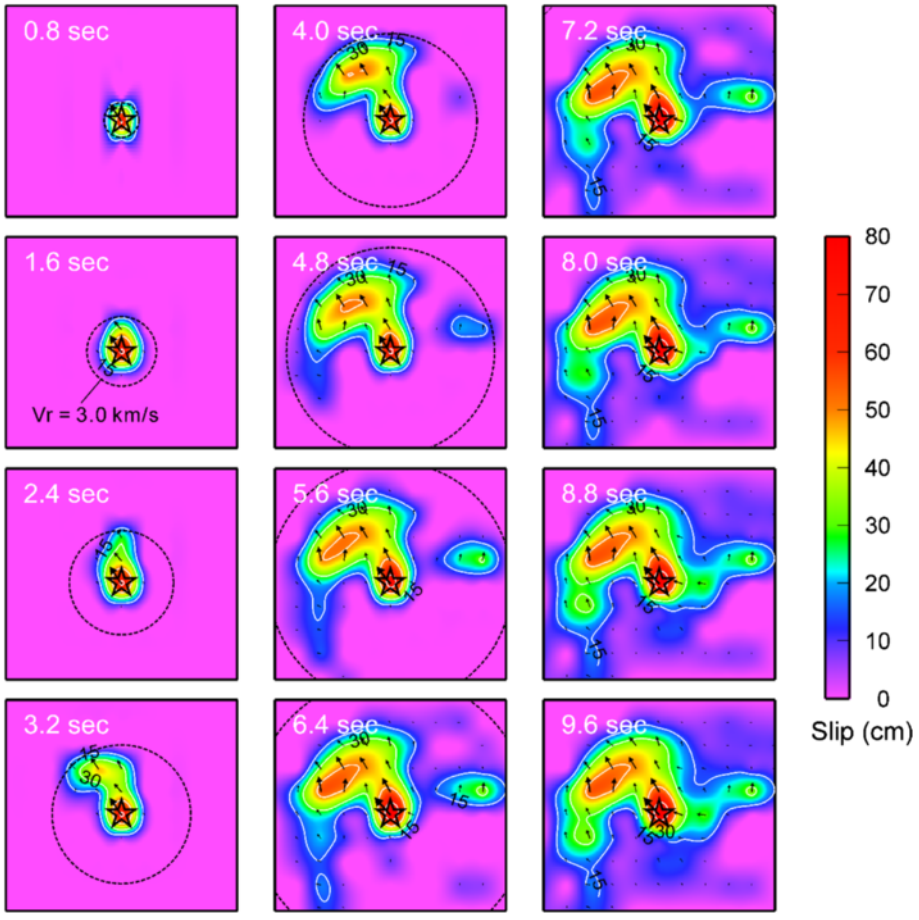

Fig. 5 Snapshot of the rupture process. Cumulative slip as a function of time is shown from *left* to *right* panels. The *dotted open circle* indicates a reference rupture front ($V_r = 3.0$ km/s). The *star* indicates the hypocenter reported by the CWB. *Vectors* indicate the slip direction and the amount of cumulative slip on each subfault

arrived at Taipei, and the seismic wave had been amplified as a result of the basin amplification effect. After that, at approximately 35 s, the slower but stronger S wave propagated into the Taipei basin. Again, the basin effect amplified the S wave, which caused large shaking in Taipei. In the same time period, the surface wave (Rayleigh wave) began to develop in the Yilan plain and its offshore area. Although these surface waves were outside the Taipei basin, their amplitude appears to be enlarged in a northwesterly direction from the epicenter. When these surface waves propagated into the Yilan plain (at around 35 s) and the Taipei basin (at around 45 s), the amplitudes had been amplified further and caused very large long-period strong ground motions, especially in Taipei City. The amplified long period ground shaking in the Taipei basin had a very long duration time of about 40 s, which lasted from 35 to 80 s. On the contrary, the ground motions in central and southern Taiwan were relatively small.

It is noted that when seismic waves propagate through the offshore seabed and mountainous areas on land, scattered seismic waves produced by steep bathymetry and topography can be observed, especially at the Ryukyu trench. The sudden change in depth of the seabed across the Ryukyu trench produced strong scattered seismic waves parallel to the trench. This phenomenon can be observed clearly between approximately 25 and 70 s. These scattered waves were then propagated toward the north and south, and parts of them propagated through the island of Taiwan, which prolonged the ground shaking further, especially in northern Taiwan.

A comparison between the norm of all three components of the observed peak ground acceleration (PGA) and the simulated ShakeMap is shown in Fig. 9. The PGA observations were compiled from the CWB 24-bit Real-time Seismic Monitoring Network. The observations were low-pass filtered using a corner frequency of 0.625 Hz to compare results with the simulated ShakeMap

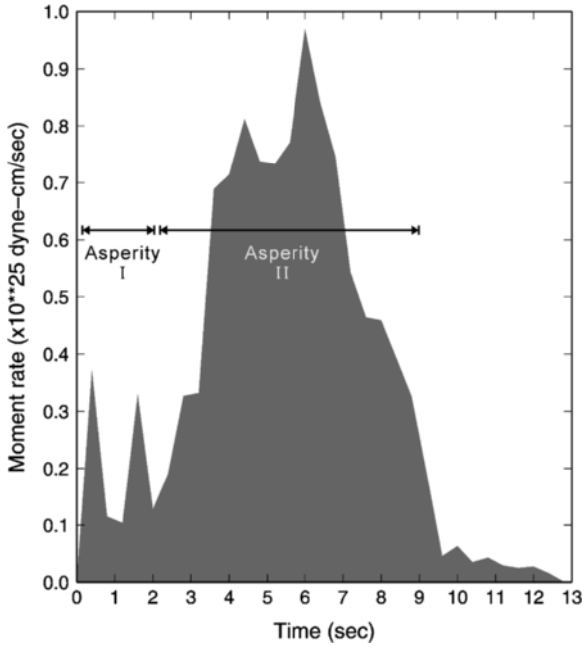

Fig. 6 Moment rate function of the 0420 earthquake

determined by a frequency ≤0.625 Hz. It is worth noting that the PGA on the seabed can also be investigated on a ShakeMap derived by numerical simulation. The results indicate that most of the characteristics of the distribution of PGA on land were essentially reproduced from the simulation. Due to the amplification of sedimentary deposits, records in the Yilan and the Taipei basin areas displayed large PGAs. This phenomenon is evident in the observations and was reproduced by the synthetic ShakeMap. However, the simulated ShakeMap appears not to have been sufficiently amplified in western Taiwan, where a thick sedimentary plain is deposited. From the numerical ShakeMap, large PGAs were further identified in the areas on the seabed north and south of the epicenter and extended northwestward toward northern Taiwan.

Discussion

Island-wide waveform comparison

Comparisons between the ground motion data of the CWB 24-bit Real-time Seismic Monitoring Network and the forward synthetic waveforms calculated from the inverted source model are provided in Fig. 10. Results show that most of the characteristics of synthetic waveforms were comparable to the observations for the

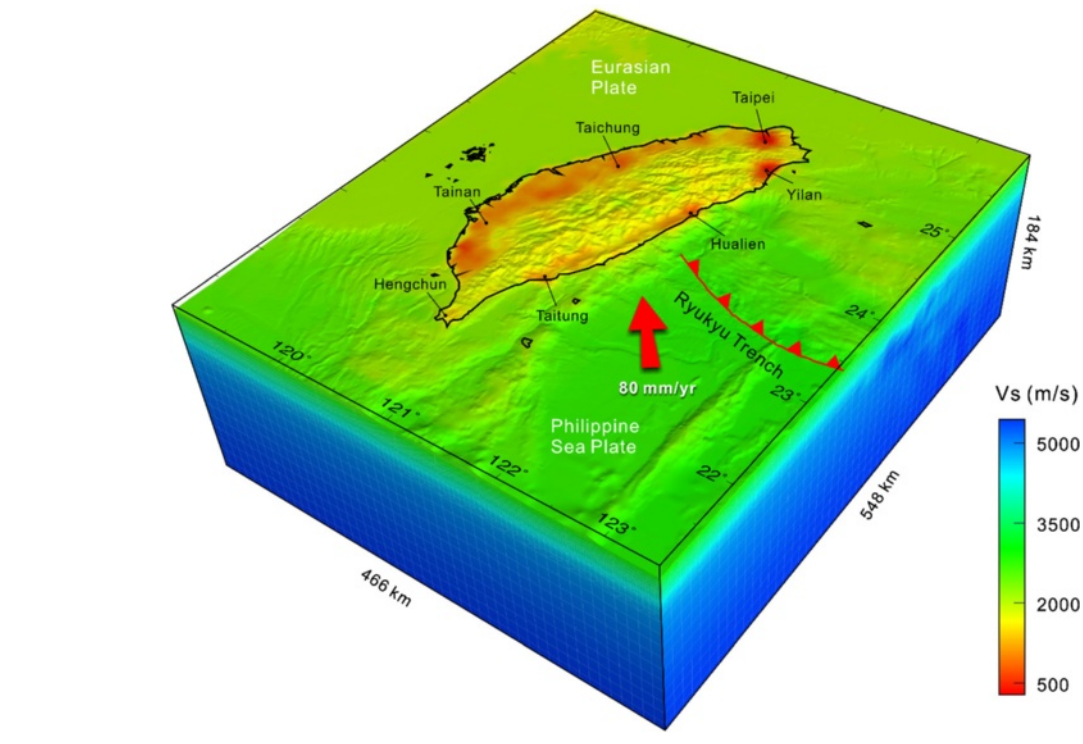

Fig. 7 Spectral-element mesh model. The size of the region is 466.01 × 548.39 km horizontally and +3.93 to −180.00 km vertically. This model covers most of the land and offshore areas of Taiwan, which is capable of handling large earthquakes from offshore regions like 0420 event. Most of the currently available relevant seismological and geological information have incorporated in the model, including surface topography, shallow sedimentary (V_s 30; Kuo et al., 2012), and large-scale 3D wave-speed heterogeneity information (Huang et al., 2014). *Background colors* show the V_s velocity, the slowest V_s in the mesh is 443 m/s

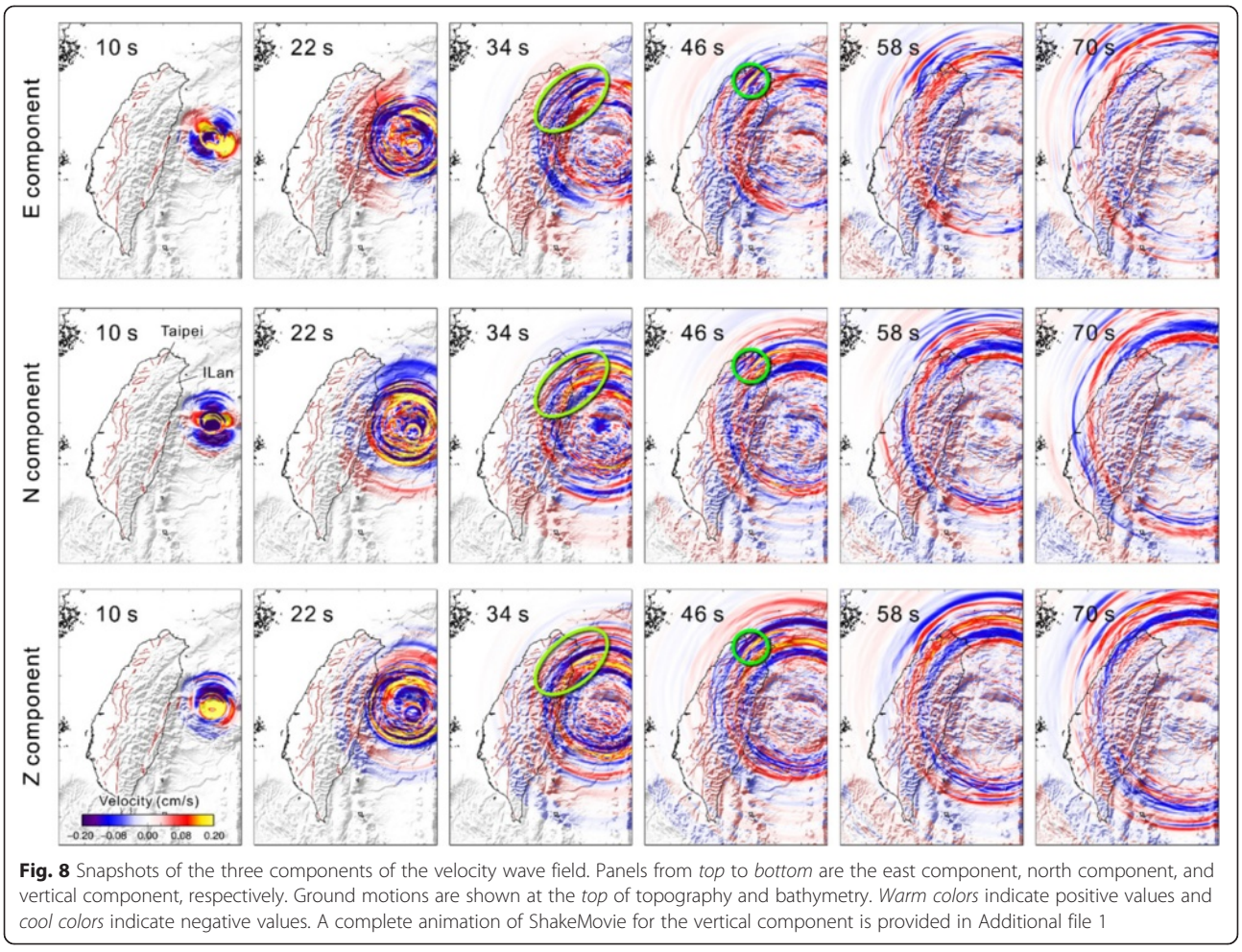

Fig. 8 Snapshots of the three components of the velocity wave field. Panels from *top* to *bottom* are the east component, north component, and vertical component, respectively. Ground motions are shown at the *top* of topography and bathymetry. *Warm colors* indicate positive values and *cool colors* indicate negative values. A complete animation of ShakeMovie for the vertical component is provided in Additional file 1

period between 10 and 50 s. The waveforms observed in northern Taiwan (e.g., stations TWB1, TWY, TWC) are generally characterized by stronger amplitudes and less complex later phases compared to those in eastern, western, and southern Taiwan. Some uncertainties in velocity structures cause greater discrepancies in the forward synthetic waveforms compared to the observations in several areas. For example, the shallow low-velocity sedimentary deposit in western Taiwan may have played an important role in amplifying the ground shaking, especially for the later reflections and surface waves (e.g., stations TCU, WCHH, CHN8). For stations in eastern Taiwan (e.g., stations TWD, HWA, EGFH), complex structures, including the detailed plate boundary of the Longitudinal Valley and Ryukyu subduction zone, were not well explained by the large-scale velocity model used (Huang et al., 2014). On the other hand, the large amplitudes of the waveforms in northern Taiwan were well modeled by the forward synthetics. The overall waveform misfit of the forward modeling is 0.49. This acceptable waveform fitting indicates that both the details of the source rupture models and the large-scale 3D velocity model are adequate to reproduce the main characteristics of the low-frequency strong ground motions of the 0420 event for simulations accurate to 0.1 Hz.

In order to obtain higher frequency (>1 Hz) ground motion simulation and synthetic waveforms, a more precise 3D velocity model will be required. Indeed, there are several important structures that will need to be confirmed by the next generation of tomographic studies, for example, shallow sedimentary structures, the exact plate boundary and the Moho depth distribution beneath Taiwan. Thus, building accurate numerical wave-speeds and structure models for Taiwan will continue to be a topic of future interest.

Long-period strong ground motion in northern Taiwan

The seismic intensity in Taipei City (150 km from the epicenter) during the 0420 event was 4 (25–80 gal, defined by CWB intensity scale), which is comparable to that observed in Yilan (intensity 4) and Hualien (intensity 4), even though the epicentral distance to the city was approximately twice that of these areas. From wave propagation snapshots (see Fig. 8 and Additional file 1),

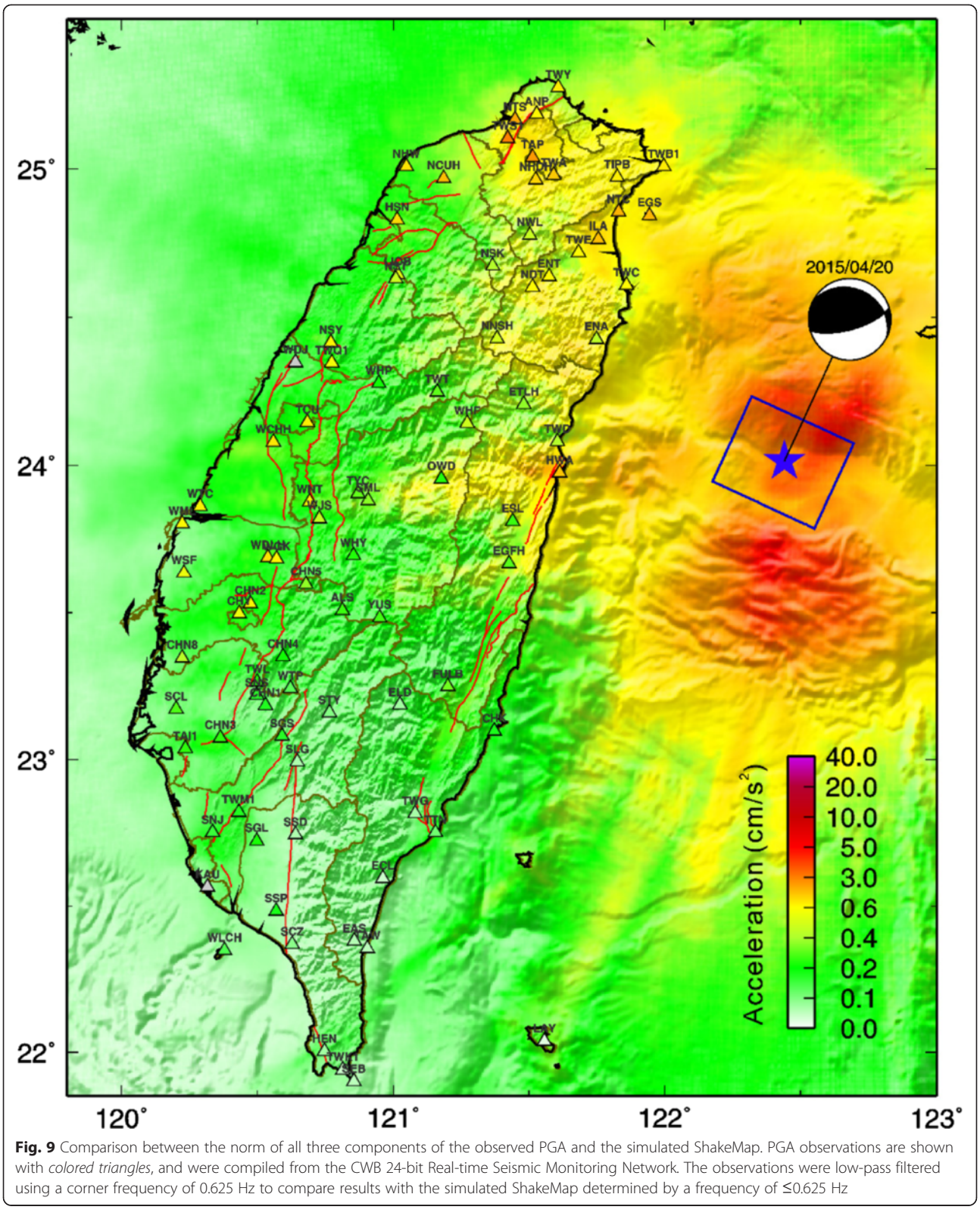

Fig. 9 Comparison between the norm of all three components of the observed PGA and the simulated ShakeMap. PGA observations are shown with *colored triangles*, and were compiled from the CWB 24-bit Real-time Seismic Monitoring Network. The observations were low-pass filtered using a corner frequency of 0.625 Hz to compare results with the simulated ShakeMap determined by a frequency of ≤0.625 Hz

it can be seen that the seismic waves were amplified when they propagated through the Taipei basin (green circles as shown in Fig. 8 at 46 s). However, relatively large S wave and surface waves were also found in northern Taiwan before they propagated into Taipei (as indicated by the light green ellipse in Fig. 8 at 34 s). The

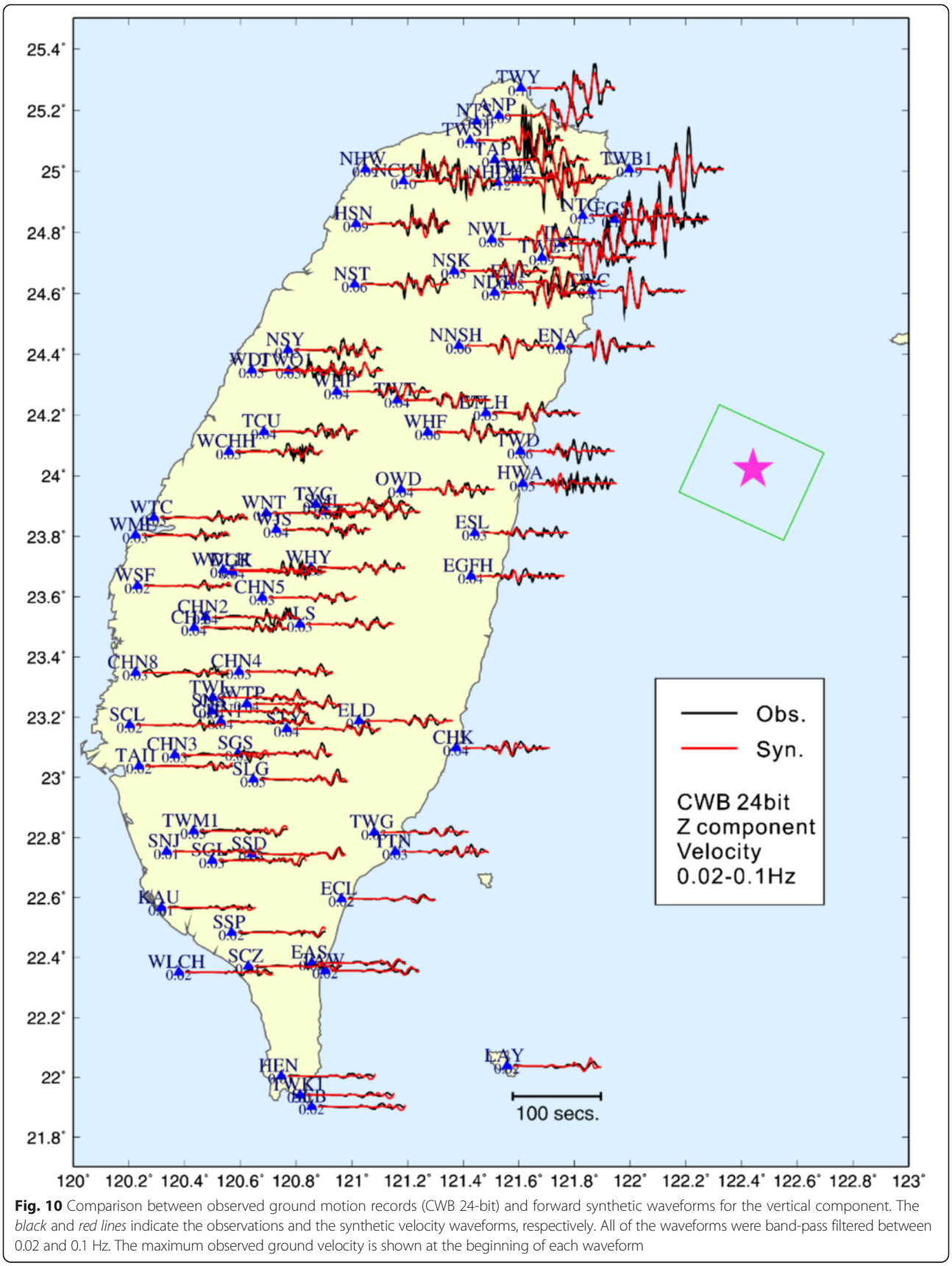

Fig. 10 Comparison between observed ground motion records (CWB 24-bit) and forward synthetic waveforms for the vertical component. The *black* and *red lines* indicate the observations and the synthetic velocity waveforms, respectively. All of the waveforms were band-pass filtered between 0.02 and 0.1 Hz. The maximum observed ground velocity is shown at the beginning of each waveform

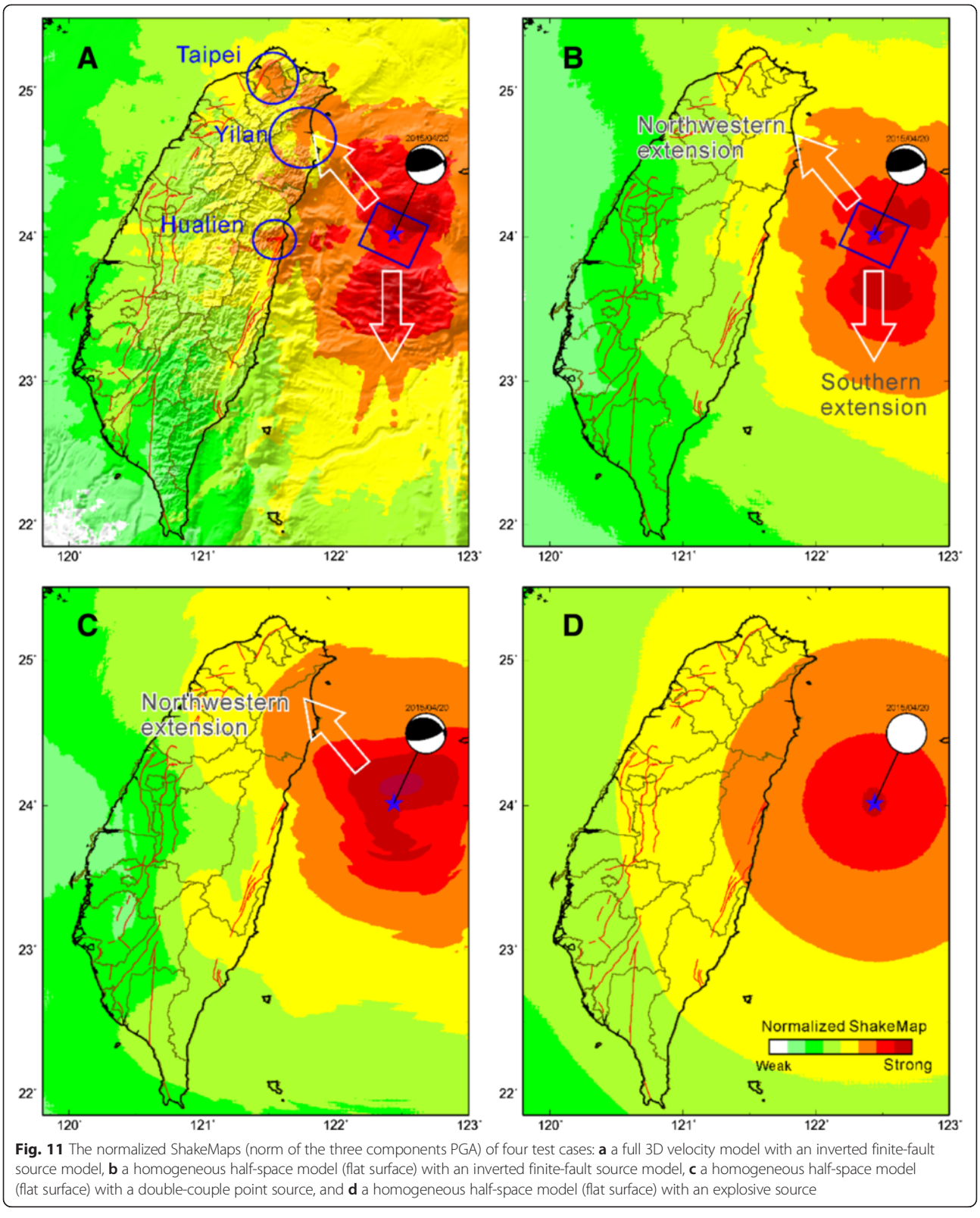

Fig. 11 The normalized ShakeMaps (norm of the three components PGA) of four test cases: **a** a full 3D velocity model with an inverted finite-fault source model, **b** a homogeneous half-space model (flat surface) with an inverted finite-fault source model, **c** a homogeneous half-space model (flat surface) with a double-couple point source, and **d** a homogeneous half-space model (flat surface) with an explosive source

amplified ground motion could be due to several factors, including path effects (e.g., basin amplification, structure focusing, and so on) and source effects (e.g., source radiation and rupture directivity). In order to clarify which factor dominates waveform amplification in northern Taiwan as well as in Taipei, a forward simulation test was

performed that considered four different cases: (A) a full 3D velocity model with an inverted finite-fault source model, (B) a homogeneous half-space model (flat surface) with an inverted finite-fault source model, (C) a homogeneous half-space model (flat surface) with a double-couple point source, and (D) a homogeneous half-space model (flat surface) with an explosive source.

The ShakeMaps of the four test cases are shown in Fig. 11. In cases A and B, a north–south extension pattern in the source area can be observed. The large ground shaking also extended to northern Taiwan, but localized strong shakings were not observed in case B, such as the Taipei basin, the Yilan plain, and the Hualien area. For the result of the point source considered in case C, the strong shaking was concentrated in the area north of the epicenter, and the northwestern extension could still be observed in northern Taiwan. For the explosive source used in case D, the result showed a concentric circular distribution centered on the epicenter. This result reflects a simple geometric decay of seismic waves as they propagate through a homogeneous half-space material.

A comparison between case A (3D velocity model) and case B (half-space model) indicates that the localized strong ground shakings in the Taipei basin and Yilan plain could be due to the low velocity sedimentary deposits; the strong motion that occurred in the Hualien area might result from complex path effects, such as sedimentary deposits in Longitudinal Valley, topographic scattering (Lee et al., 2009), or subducting structures (Furumura and Kennett, 2005; Chen et al., 2013). A stronger ShakeMap pattern can be observed between Yilan and Hualien in case A compared to that in case B. This might be due to the topographic effect which could cause amplified ground motion at tops and ridges of mountain (Lee et al., 2009). The finite-fault ruptured from the deep to the shallower subduction zone (from north to south) also caused a remarkable directivity effect, which produced a southern-extension ShakeMap pattern from the epicenter in cases A and B, but it was not present in case C. It is noted that a northwesterly strong-motion extension can be found in both the finite-fault model (cases A and B) and the double-couple point source (case C), compared to that with a simple geometric decay (explosive source in case D) where there is no such extension. This implies that the source effect, especially the radiation pattern, is one of the dominant factors that caused strong ground shaking in northern Taiwan.

Large forearc sedimentary basins (Hoping basin, Nanao basin, and East-Nanao basin) developed along the southwestern Ryukyu Trench could also amplify the ground motions. These forearc structures are not included in the 3D velocity model. In previous studies about the Taipei basin (Lee et al., 2008, 2009), the seismic wave amplification due to the basin effect is obvious for sites located in the basin. Outside the basin, the amplification is not apparent. Only second-order effects, such as reflections and scattering waves resulted from basin boundary can be found. These effects are minor that do not contribute much to the peak ground motion. This might also be true for the forearc basins which could amplify shaking in offshore sedimentary basins, but this effect will not contribute to the large ground motions observed in northern Taiwan.

From these results, it can be deduced that the strong ground shaking in Taipei during the 0420 earthquake was mainly caused by two factors: (1) Taipei basin amplification and (2) source radiation.

Conclusions

The 0420 event caused a long-period strong ground shaking in Taipei City, which is not only due to the basin effect but also the source radiation. On 31 March 2002, an M_w 7.1 earthquake, called the 331 Hualien offshore earthquake, also occurred in this area (see Fig. 1). Again, although the hypocentral distance to Taipei City was more than 100 km, people in Taipei felt a very strong long-period ground shaking for more than 30 s. The focal mechanism of this event is similar to that of the 0420 earthquake, which might be related to the subduction zone structure. These events imply that the southernmost Ryukyu subduction zone earthquakes that occurred in offshore eastern Taiwan could be a critical issue for seismic hazard assessment in northern Taiwan.

The seismic hazards resulting from long-period ground motions have been observed in several large subduction zone events, such as the 1985 Michoacan M8.1, Mexico earthquake (Anderson et al., 1986; Mendoza and Hartzell, 1989) and the 2011 Tohoku M9.0 earthquake in Japan (Takewaki et al., 2011; Maeda et al. 2013). Hsu et al. (2012) inverted the slip-deficit rates and the geometric configuration of the southernmost Ryukyu subduction zone. Their preferred fault model dips 10° northward and extends around 70 km from the Ryukyu Trench to a depth of 13 km. The slip deficit rate exhibits a left-lateral motion of 78 mm/year and a normal motion of 36 mm/year on a 290° striking fault. This fault geometry is similar to the focal mechanism of 0420 event, having a strike of 295° and dipping 26° toward north.

As known from the source inversion results in this study, the events that occurred at the southernmost Ryukyu subduction zone could have mainly ruptured in the northwest-to-southeast direction, with right-lateral thrust and updip movements on the north-dipping subducting plate boundary. This source mechanism can cause a striking source radiation effect, which amplifies the shaking on the northwestern side from the source area. It leads to large ground motions propagating toward northern Taiwan and will be further amplified by

the basin effect, as was observed in Taipei City during the 0420 earthquake. Thus, the type of subduction zone event that occurred in offshore eastern Taiwan should be seriously considered in future earthquake scenario analyses for the purposes of seismic hazard assessment.

Additional file

Additional file 1: 3D wave propagation of the 0420 earthquake. This movie is an animation of the simulation result for the vertical components of the velocity wavefield. The simulation was based on the spectral-element method carried out on IES Green cluster. (MP4 64809 kb)

Competing interests
The author declares that he has no competing interests.

Authors' contributions
SJ analyzed the simulated and observed waveform data, conducted the numerical inversion and forward simulation. The author drafted and approved this manuscript.

Acknowledgements
The 24-bit real-time strong motion data for this paper are available from the Taiwan Rapid Earthquake Information Release System implemented by the Central Weather Bureau. The teleseismic data used were obtained from Incorporated Research Institutions for Seismology (IRIS). This research was supported by Academia Sinica, funded through the Taiwan Numerical Earthquake Model (TNEM) project, Grant Number 102-Investigator Award-02. This research was also supported by the Taiwan Earthquake Research Center, funded through the Ministry of Science and Technology by Grant Number MOST 103-2628-M-001-004-MY3. The TEC contribution number for this article is 00116.

Received: 31 July 2015 Accepted: 1 October 2015
Published online: 08 October 2015

References
Allmann BP, Shearer PM (2009) Global variations of stress drop for moderate to large earthquakes. J Geophys Res 114:B01310

Anderson JG, Bodin P, Brune JN, Prince J, Singh SK, Quaas R, Onate M (1986) Strong ground motion from the Michoacan, Mexico, earthquake. Science 233(4768):1043–1049

Bjerrum LW, Sørensen MB, Atakan K (2010) Strong Ground-motion simulation of the 12 May 2008 Mw 7.9 Wenchuan earthquake, using various slip models. Bull Seismol Soc Am 100(5B):2396–2424

Brocher TM (2005) Empirical relations between elastic wavespeeds and density in the Earth's crust. Bull Seismol Soc Am 95(6):2081–2092

Chen K-C (2003) Strong ground motion and damage in the Taipei basin from the Moho reflected seismic waves during the March 31, 2002, Hualien, Taiwan earthquake. Geophys Res Lett 30(11). doi:10.1029/2003GL017193.

Chen Y-L, Shin T-C (1998) Study of the earthquake location of 3-D velocity structure in Taiwan area. Meteoritical Bulletin 42:135–169

Chen K-H, Kennett B, Furumura T (2013) High frequency waves guided by subducted plates underneath Taiwan and their association with seismic intensity anomalies. J Geophys Res 118:665–680. doi:10.1029/2012JB009691

Furumura T, Kennett BLN (2005) Subduction zone guided waves and the heterogeneity structure of the subducted plate: Intensity anomaly in northern Japan. Geophys Res 110. doi:10.1029/2004JB003486.

Hartzell SH, Heaton TH (1983) Inversion of strong ground motion and teleseismic waveform data for the fault rupture history of the 1979 Imperial Valley, California earthquake. Bull Seismol Soc Am 73:1553–1583

Hsu Y-J, Ando M, Yu S-B, Simons M (2012) The potential for a great earthquake along the southernmost Ryukyu subduction zone. Geophys Res Lett 39:L14302. doi:10.1029/2012GL052764

Huang Y-L, Huang B-S, Wen K-L, Lai Y-C, Chen Y-R (2010) Investigation for strong ground shaking across the Taipei basin during the M_W 7.0 eastern Taiwan offshore earthquake of 31 March 2002. Terr Atmos Ocean Sci 21:485–493

Huang H-H, Wu Y-M, Song X, Chang C-H, Lee S-J, Chang T-M, Hsieh H-H (2014) Joint Vp and Vs tomography of Taiwan: implications for subduction-collision orogeny. Earth Planet Sci Lett 392:177–191

Kanamori H, Anderson DL (1975) Theoretical basis of some empirical relations in seismology. Bull Seisrnol Soc Amer 65:1073–1095

Kennett BLN, Engdahl ER (1991) Traveltimes for global earthquake location and phase identification. Geophys J Int 122:429–465

Kikuchi M, Kanamori H (1982) Inversion of complex body waves. Bull Seismol Soc Am 72:491–506

Komatitsch D, Tromp J (1999) Introduction to the spectral-element method for 3-D seismic wave propagation. Geophys J Int 139:806–822

Komatitsch D, Liu Q, Tromp J, Süss P, Stidham C, Shaw JH (2004) Simulations of ground motion in the Los Angeles basin based upon the spectral-element method. Bull Seismol Soc Am 94:187–206

Kuo C-H, Wen K-L, Hsieh H-H, Lin C-M, Chang T-M, Kuo K-W (2012) Site classification and Vs30 estimation of free-field TSMIP stations using the logging data of EGDT. Eng Geol 129–130:68–75

Lee S-J, Ma K-F, Chen H-W (2006) Three-dimensional dense strong motion waveform inversion for the rupture process of the 1999 Chi–Chi, Taiwan, earthquake. J Geophys Res 111:B11308

Lee S-J, Chen H-W, Huang B-S (2008) Simulation of strong ground motion and 3D amplification effect in the Taipei Basin by using a composite grid finite-difference method. Bull Seis Soc Am 98:1229–1242. doi:10.1785/012/0120060098

Lee S-J, Komatitsch D, Huang B-S, Tromp J (2009) Effects of topography on seismic wave propagation: an example from northern Taiwan. Bull Seis Soc Am 99:314–325. doi:10.1785/0120080020

Lee S-J, Liang W-T, Cheng H-W, Tu F-S, Ma K-F, Tsuruoka H, Kawakatsu H, Huang B-S, Liu C-C (2013) Toward real-time regional earthquake simulation I: real-time moment tensor monitoring (RMT) for regional events in Taiwan. Geophys J Int. doi:10.1093/gji/ggt371

Lee S-J, Huang H-H, Shyu JBH, Lin TC, Yeh TY (2014) Numerical earthquake model of the 31 October 2013 Ruisui, Taiwan, Earthquake: source rupture process and seismic wave propagation. J Asian Earth Sci 96:374–385. doi:10.1016/j.jseaes. 2014.09.020

Lin J-Y, Sibuet J-C, Hsu S-K, Wu W-N (2014) Could a Sumatra-like megathrust earthquake occur in the south Ryukyu subduction zone? Earth Planets Space 66:49. doi:10.1186/1880-5981-66-49

Maeda T, Furumura T, Noguchi S, Takemura S, Sakai S, Shinohara M, Iwai K, Lee S-J (2013) Seismic and tsunami wave propagation of the 2011 Off the Pacific Coast of Tohoku Earthquake as inferred from the tsunami-coupled finite difference simulation. Bull Seism Soc Am 103(2B):1456–1472. doi:10.1785/0120120118

Mendoza C, Hartzell SH (1989) Slip distribution of the 19 September 1985 Michoacan, Mexico, earthquake: near-source and teleseismic constraints. Bull Seismol Soc Am 79(3):655–669

Nakamura M (2014) Seismic structure of subducted oceanic crust near the slow-earthquake source region in the southern Ryukyu arc. Earth Planets Space 66:96. doi:10.1186/1880-5981-66-96

Sørensen MB, Atakan A, Pulido N (2007) Simulated strong ground motions for the great M 9.3 Sumatra-Andaman Earthquake of 26 December 2004. Bull Seism Soc Am 97:S139–S151

Takewaki I, Murakami S, Fujita K, Yoshitomi S, Tsuji M (2011) The 2011 off the Pacific coast of Tohoku earthquake and response of high-rise buildings under long-period ground motions. Soil Dyn Earthq Eng 31(11):1511–1528

Wu Y-M, Shyu JBH, Chang C-H, Zhao L, Nakamura M, Hsu S-K (2009) Improved seismic tomography offshore northeastern Taiwan: implications for subduction and collision processes between Taiwan and the southernmost Ryukyu. Geophys J Int 178:1042–1054